

Simulation of radiation damages in molybdenum by combining molecular dynamics and OKMC

Gui-Yan Wu¹ · Neng-Wen Hu² · Hui-Qiu Deng¹ · Shi-Fang Xiao¹ · Wang-Yu Hu²

Received: 3 November 2015 / Revised: 2 March 2016 / Accepted: 8 April 2016 / Published online: 30 November 2016
© Shanghai Institute of Applied Physics, Chinese Academy of Sciences, Chinese Nuclear Society, Science Press China and Springer Science+Business Media Singapore 2016

Abstract In this paper, radiation defects in bcc molybdenum with the primary knock-on atom (PKA) energies of 2–40 keV are simulated by the molecular dynamics. The binding energy of single point defect-to-defect clusters increases with the cluster size. The stability and mobility of point defects and defect clusters are analyzed. The interstitial-type clusters are found to be easily migrating along the $\langle 111 \rangle$ direction with low barriers (0.01–0.10 eV). Then, the object kinetic Monte Carlo is used to gain insight into the long-term defect evolution in the cascade. The simulation results indicate that Stage I almost occurs at annealing temperature of 100 K, which corresponds to the correlated recombination resulting from the motion of small interstitial clusters ($n \leq 2$). The formation of sub-stage partly as result of the small vacancy clusters motion. At about 460 K, the Stage II starts because of uncorrelated recombination due to an emitting mechanism of larger clusters. Size distribution of the clusters at the cascade quenching stage is positively correlated with the PKA energies, affecting notably the subsequent annealing process.

Keywords Displacement cascades · Molybdenum · Defects · Computer simulation

1 Introduction

With excellent high temperature strength, high melting point, good thermal conductivity, good resistance to corrosion and radiation-induced swelling in nuclear environment, molybdenum (Mo) is a promising material for innovative nuclear energy systems (fast neutron reactors, thorium-fueled molten salt reactors and fusion reactors) [1–6]. As a structural material of the first wall [7, 8], Mo will be subject to the impact of high-energy particles, hence the formation of a large number of point defects, and even defects clusters or loops. Further interaction and evolution of the clusters or loops causes microstructure changes and mechanical performance degradation, e.g., irradiation hardening, embrittlement, swelling and creep [9]. Many features of the radiation damages have been studied by TEM [10–13], but further explanations are still inaccessible, such as the mobility of self-interstitials or their clusters, the formation and mobility of the large prismatic vacancy loops and interstitial loops [14]. It is, therefore, of significance to understand the radiation damages, including the long time-scale evolution behaviors for defects and defect clusters, and predicting or assessing the material performance in applications.

For defect kinetic evolution in Mo, limited atomistic simulation and experimental data are available for the mobility model of vacancy/interstitial clusters of different sizes. To provide accessible fundamental data for large-scale molecular dynamics simulation of radiation damage, Han et al. [15] reported an extensive ab initio study of self-interstitials structures, formation energies and migration

This work was supported by the Shanghai Municipal Science and Technology Commission (No. 13ZR1448000) and the National Natural Science Foundation of China (No. 11505266).

✉ Wang-Yu Hu
wyuhu@hnu.edu.cn

¹ Department of Applied Physics, School of Physics and Electronics, Hunan University, Changsha 410082, China

² Department of Materials Science and Engineering, Hunan University, Changsha 410082, China

barriers in V and Mo. They found that the $\langle 111 \rangle$ dumbbell migration energy in Mo was 0 to within the uncertainty of the current calculation (-0.05 to 0.05 eV). This is consistent with experiments (0.05 eV) [16].

Simulations by Manh et al. [17] studied the systematic trends for the self-interstitials atom (SIA) defect behavior in bcc transition metal. They found that the $\langle 111 \rangle$ configuration was the most stable SIA defect in all the non-magnetic bcc metals. Their study concludes that group-specific trends showed by the SIA defect structures correlates with the observed thermally activated mobility of SIA defects.

Making clear the formation and evolution of defects and clusters/loops is of practical significance in reducing irradiation embrittlement. Recent studies on displacement cascades produced by 50 keV Xe ions in Mo single crystal revealed that large prismatic vacancy loop formed near the impact surface as a result of fast recrystallization, and the mobility of vacancy dislocation loops was high [14]. On the contrary, there is no indication that large SIA clusters are formed in Fe in early stage of the cascade evolution [18]. A meaningful database of the point defect survival efficiency and partitioning probability into different sized clusters was obtained by Selby et al. [19], but mobility of vacancy/SIA clusters in Mo remains unevaluated.

Molecular dynamics (MD) is a useful tool for studying the primary damage produced by high-energy displacement cascades and analyzing the migration mechanism of defects. The main characteristics of defect evolution can be predicted using object kinetic Monte Carlo (OKMC). Combining OKMC with MD is a feasible solution to perform atomistic level simulation of the microstructure evolution. This multi-scale technique has been successfully employed to describe the long time evolution of the defects in bcc Fe [20, 21], fcc Cu [22], Ni [23] and 3C-SiC [24]. In their study on evolution of the defect distribution and how the cascade defect distribution evolves in diffusion process, Heinisch and Singh [25] reported that the spatial segregation, and clustering of the vacancies and SIAs, contributed to a differential production of mobile vacancies and SIAs, with strong temperature dependence. However, the inmost law and mechanisms for defect clusters and loops interactions are still not clear.

In this paper, we report our annealing simulations of radiation-induced damage in bcc molybdenum based on a reliable MD database with PKA (Primary knock-on atom) energies of 2–40 keV. Specifically, we aim to address the following issues: (1) the defect production and the size distribution of defects clusters; (2) the stability and migration behavior of vacancy/SIA clusters; and (3) the annealing of damage as a function of temperature for cascade. This study provides qualitative and quantitative

reference information to predict the microstructure evolution of materials under irradiation.

2 Methodology

Molecular dynamics were performed to study displacement cascades in Mo with modified MOLDY codes. A modified analytical embedded-atom method (MAEAM) potential was employed for describing the Mo–Mo interaction. Details of the specific formalisms can be found in Ref. [26]. The process of simulating the cascade damage production involved setting up a simulation box of pure molybdenum, sized at $60a_0 \times 60a_0 \times 60a_0$ (totally 432,000 atoms), where a_0 is the lattice parameter of body-centered cubic (bcc) Mo bulk. The system was equilibrated at 100 K and 300 K for 10 pico-s. PKA energies of 2, 5, 10, 20, 40 and 60 keV were chosen along the $\langle 135 \rangle$ orientation, so as to avoid channeling effect. Periodic boundary conditions were applied for all the MD simulations.

The MD results are essential for OKMC simulations. The migration energies and dissociation energies (the sum of binding and migration energies) of the defect clusters were implemented as key input parameters in kinetic model. The binding energies were obtained by MD method using MAEAM potential [27], and the migration energies, by NEB (nudged elastic band) [28, 29], an efficient method for finding MEPs (minimum energy path) [30] between the given initial state and final state (equilibrium configurations). The MEP was found by constructing a set of images (25 images, including two stable images) between the initial and final state.

The OKMC simulation method is capable of tracking the evolution of defects at longer time-scale. In the model, the point defects (vacancies, interstitials and their clusters) were treated as “objects.” The objects may migrate, emit and interact with each other, which are defined as “internal event” (migration, recombination, dissociation and annihilation) [31–35]. Definitely, a recombination event happens when one object encounters its opposite type. If the object is large enough to allow point defect emission, a dissociation event occurs.

The probabilities $\Gamma_{n,i}$ of migration jumps and emissions (for object n and event i) are given by [36, 37]

$$\Gamma_{n,i} = v_{n,i} \exp[-E_{a,n,i}/(kT)], \quad (1)$$

where $v_{n,i}$ is attempt frequency, $E_{a,n,i}$ is the corresponding dissociation energy, k is the Boltzmann’s constant and T is the absolute temperature. According to the probabilities $\Gamma_{n,i}$ the average time step length is given by Ref. [38]

$$\Delta t = -\ln \xi / k_{\text{tot}}, \quad (2)$$

where k_{tot} is the sum of probabilities of all the events and ζ is a random number in the range between zero and one.

The defect configuration obtained from MD simulations was introduced in the center of the KMC simulation box of Mo bulk, sized at $(120a_0)^3$. The damage annealing simulation was performed for all cascades, and the system was annealed at temperatures from 30 K to 1000 K for a given period of time. The temperature interval was $\Delta T_{j+1} = 0.05T_j$, ($j = 1, 2, 3, \dots$). The annealing at each temperature was repeated for 50 times. We assumed that larger vacancy clusters (>4) were immobile.

3 Results and discussion

3.1 The distribution of point defects

Consistent with previous works [19], the number of point defects shortly increased and then decreased due to the interstitials recombining with vacancies. Then, it almost remains stable. It was worth noting that the sub-cascades were observed at the PKA energy of 40 keV. As shown in Table 1, the temperature and PKA energy significantly affect the production and recombination of defects. Higher temperature and PKA energy induced more defects and larger clusters and delayed the time to enter thermal peak stage. At $T = 100$ K, for example, the maximum number of defects is $N_{\text{d-max}} = 658$ and the time to entering thermal peak stage is $t_{\text{peak}} = 0.342$ ps at $E_{\text{PKA}} = 2$ keV; while they are $N_{\text{d-max}} = 90314$ and $t_{\text{peak}} = 1.662$ ps at $E_{\text{PKA}} = 40$ keV. This was probably because the mobility of atoms increases at higher temperature and PKA energy, which hinder recombination of the point defects.

The size (defined by the number of point defects contained) distribution of clusters and defects distribution of the system at $T = 100$ K and 300 K are shown in Fig. 1. It can be seen that most of the clusters were composed of just one or two defects, and large vacancy clusters could be dispersed in the high temperature cascade. Comparing

Table 1 Time to enter thermal peak stage (t_{peak}), maximum number of defects ($N_{\text{d-max}}$) and residual Frenkle pairs (N_{FP}) at different PKA energies and temperatures

E_{PKA} (keV)	t_{peak} (ps)		$N_{\text{d-max}}$		N_{FP}	
	100 K	300 K	100 K	300 K	100 K	300 K
2	0.342	0.410	658	696	11	15
5	0.408	0.463	1650	1784	48	49
10	0.461	0.840	3434	5167	74	77
20	0.755	1.143	8233	17,187	139	199
40	1.662	1.590	90,314	60,652	567	486

Fig. 1a–d, the surviving defects clusters generated by high recoil energies are larger than those by the lower energies. In addition, three configurations single interstitials were observed in simulation including $\langle 111 \rangle$ oriented crowdions, $\langle 110 \rangle$ and $\langle 111 \rangle$ direction dumbbells. The most stable interstitial in Mo is the $\langle 111 \rangle$ dumbbells, which can easily move along the $\langle 111 \rangle$ direction. This is consistent with previous GGA and LDA results [14, 15].

3.2 The migration and binding energies of interstitial/vacancy clusters

The most important parameter for OKMC simulations is the migration energies, which can be obtained by the NEB method, as listed in Table 2. The initial and final states must be specified as searching the saddle point; therefore, the migration direction, equilibrium configuration and migration barrier should be included. In terms of migration direction, the NEB may be only appropriate for single vacancy and small size interstitial clusters. We built the configurations as many as possible and kept the one having higher binding energy and lower formation energy as the most stable configuration. The migration barriers were calculated by NEB method in a box sized at $(10a_0)^3$, where it was relaxed for 10 ps under 0 K. Several equilibrium configurations for vacancy clusters in bcc were defined in Ref. [40, 41]. For example, the migration of mono-vacancy starts from the original point (0, 0, 0) and ended at the nearest neighbor body-centered site (0.5, 0.5, 0.5), by moving along the $\langle 111 \rangle$ direction (Fig. 2a); other clusters were calculated in a similar way. According to Fu et al. [39], the migration mechanism of vacancy clusters was simply explained by the fact that the atom at final site migrated to the initial one, recombined with one vacancy and then produced a new vacancy. Furthermore, the motion of small vacancy clusters required passing through metastable intermediate states (for instant, V_2 and V_4 , see Fig. 2b, d). The same as in other OKMC simulation [42], larger vacancy clusters (size >5) were believed to be immobile.

It should be emphasized that the migration energies of vacancy clusters are size dependent. For small size V_n clusters, the migration energies are 0.958, 1.032, 0.982 and 1.383 eV, respectively, corresponding to $n = 1, 2, 3$ and 4, as shown in Fig. 2 and Table 2. Unexpectedly, the value of V_3 is lower than V_2 and V_4 because V_3 cluster has more diversified and complicated configurations. It is interesting that the unexpected appearances are similar with ab initio calculations in iron [39] (Table 2). One possible reason is that molybdenum and iron are of the same crystal structure. In Table 2, the migration energies of interstitial I_n clusters are much less than that of V_n ones, which illustrates that the migration of I_n clusters is much easier. The migration energies of I_n clusters increased with their sizes, and an

Fig. 1 Size distribution of defect clusters at MD temperature of 100 and 300 K and E_{PKA} of 10 and 40 keV. Blue, vacancy; red, interstitial. (Color figure online)

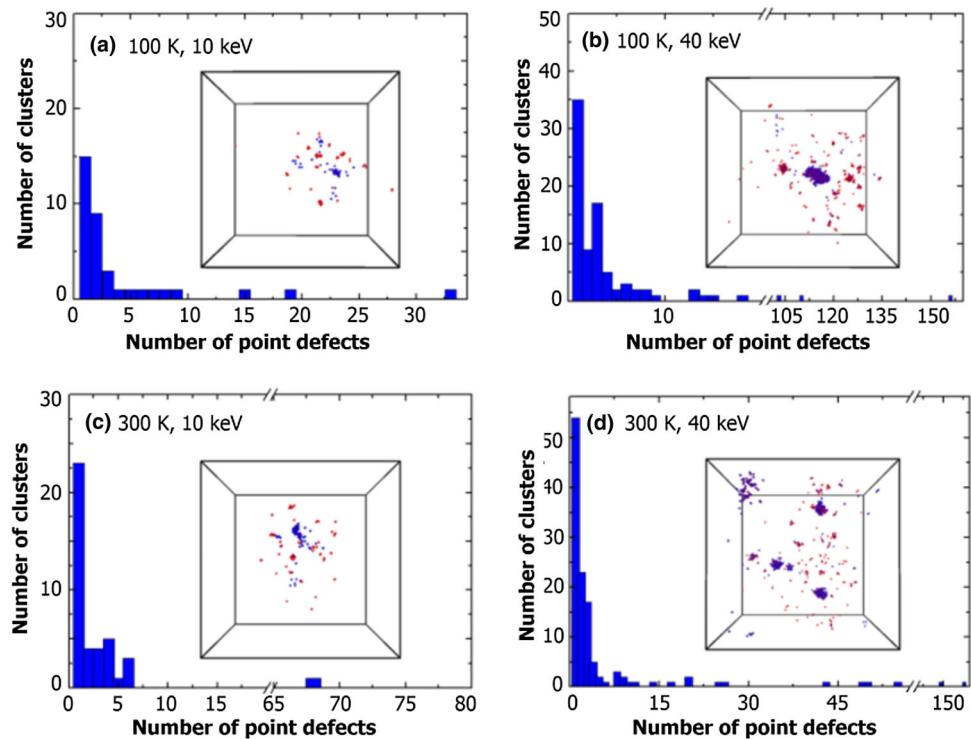


Table 2 Binding and migration energies of defect clusters

Defect type	bcc-Mo		α -Fe [39] [E_m (eV)]
	E_b (eV)	E_m (eV)	
V_1	–	0.985	0.67
V_2	0.268	1.023	0.62
V_3	0.930	0.982	0.35
V_4	1.985	1.383	0.48
V_n	$0.055n^{2.461}$	Immobile	–
I_1	–	0.009	0.34
I_2	0.349	0.012	0.42
I_3	1.006	0.141	0.43
I_4	1.647	0.113	–
I_n	–	$0.0097n^{0.0441}$	–

empirically fitted relationship, $0.0097n^{0.0441}$, was fitted. As mentioned before, searching the most stable configurations and exploring several possible migration mechanisms are essential for calculating migration energies. Notably, interstitial-type defects are found to be made of $\langle 111 \rangle$ parallel single dumbbells and believed to have special migration mechanisms (Johnson's mechanism [41]), where two atoms of the dumbbells dissociate at first, and then one of them would migrate and extrude the other atom along the migration path to produce a new dumbbell; and the left one would recover at normal lattice site. We found that the I_n clusters could easily migrate with lower migration energies (0.01–0.10 eV). The migration barriers and paths

are potted in Fig. 3. All the saddle points lied in middle of the migration path. The binding energies of defect clusters are the other energetic input data for the simulations. Their values (V_{2-4} and I_{2-4}) are determined by MD simulations with MAEAM potential. Table 2 shows that the binding energies increase with the size. The stable structures are shown in Fig. 2.

3.3 The OKMC simulation

In the OKMC simulation, the displacement cascades simulated by MD (Table 2) were used as the initial defect distribution. Cascade energies of 2, 5, 10, 20 and 40 keV were annealed. Each cascade result was introduced in the center of the OKMC box sized at $(120 a_0)^3$. During annealing, the system was simulated at temperatures of 30–1000 K and each cascade was annealed 50 times. Figure 4 shows the average number of defects as the function of annealing temperature. It is interesting that each annealing curve has typical stages for the decrease in the number of defects Stage I is around 100 K. This is the recombination stage, mainly due to the motion of interstitials clusters which were annihilated with nearby vacancy defects or larger clusters. Stage II, at 390–460 K, is related to the recombination of the uncorrelated defects. For 5 keV and 10 keV cascades formed at 100 K, Stage II occurred at 390–395 K, while it occurred at 430 K for the 100 K 40 keV cascade. There exist two mechanisms acting together on the uncorrelated recombination, the irrelative

Fig. 2 Migration energies of vacancy-type (V_1, V_2, V_3 and V_4) defects moving along the most favorable migration pathways. The x axis is the image points. The vacant sites are represented by green squares. (Color figure online)

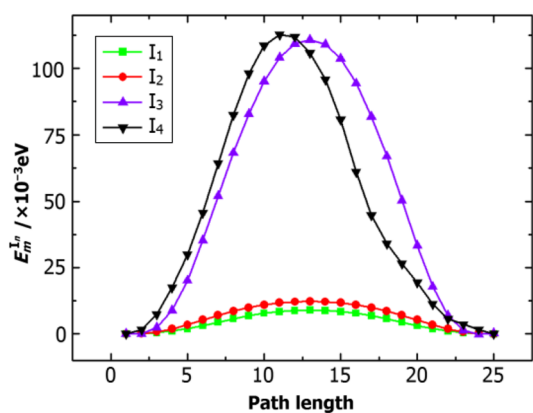
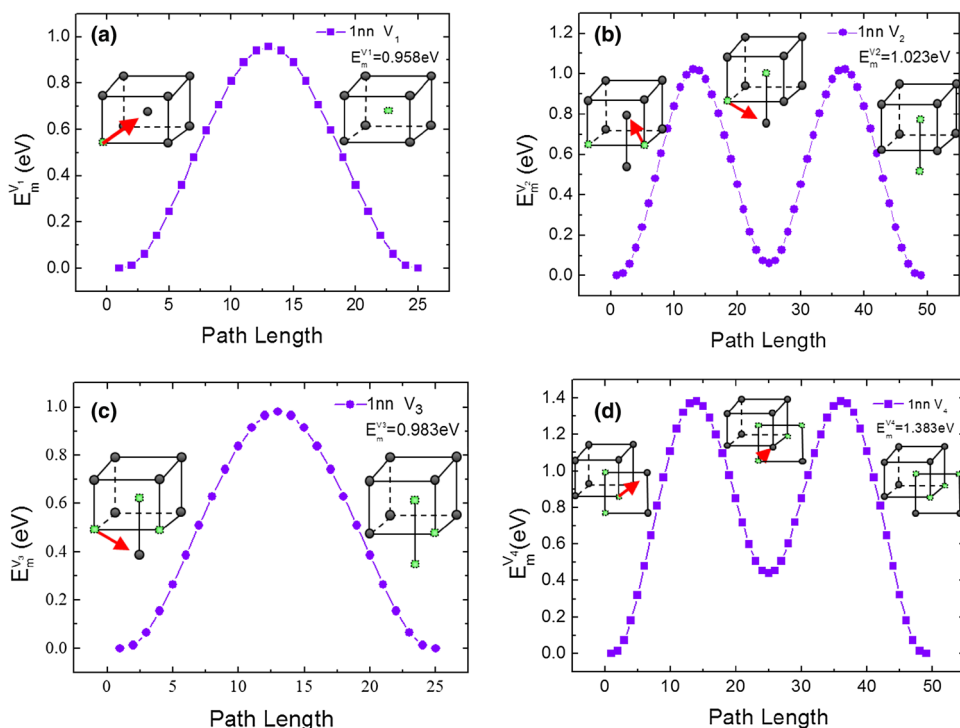


Fig. 3 Migration energies of interstitial-type (I_1, I_2, I_3 and I_4) defects along the most favorable migration pathways. The x axis is the image points

recombination of small size defects (<3), and the defects emitting from the larger size clusters. The 40 keV results are mainly due to the latter.

The most significant feature is a slight fluctuation observed in 300–600 K (Fig. 5a), where the number of defects increases first but then decreases. It declines continuously and finally reaches a stable one. This is mainly due to the emitting events during the annealing process, in which a large number of new tiny clusters are extracted, and most of them migrate to annihilate with opposite defects. Figure 5 also shows that for 2 keV cascade, the second recombination of the defects started at 537 K, being 100 K higher than those of the 20 keV cascade. This is

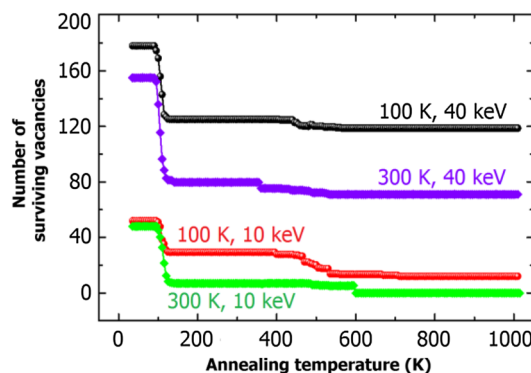


Fig. 4 Residual number of vacancies versus annealing temperature, with primary defects formed at $T = 100$ or 300 K and $E_{PKA} = 10$ or 40 keV

because that the small clusters generated at $E_{PKA} = 2$ keV completely recombine in Stage I, but larger clusters recombine at high temperatures. Note that most of small clusters occur at higher E_{PKA} , especially in Stage II. So, the temperature reduced by the energy augments.

As shown in Fig. 1, the defect distribution and cluster size are affected remarkably by PKA energies, and so is the recombination efficiency in annealing. Figure 6 shows the fraction of recombination as a function of annealing temperature. Apparently, a higher cascade temperature leads to a higher ratio of recombination, but the impact of cascade energy is otherwise. This indicates that the cascade energy is notably positively correlated with the cluster size and thus affects the annealing process. For 80% defects formed at

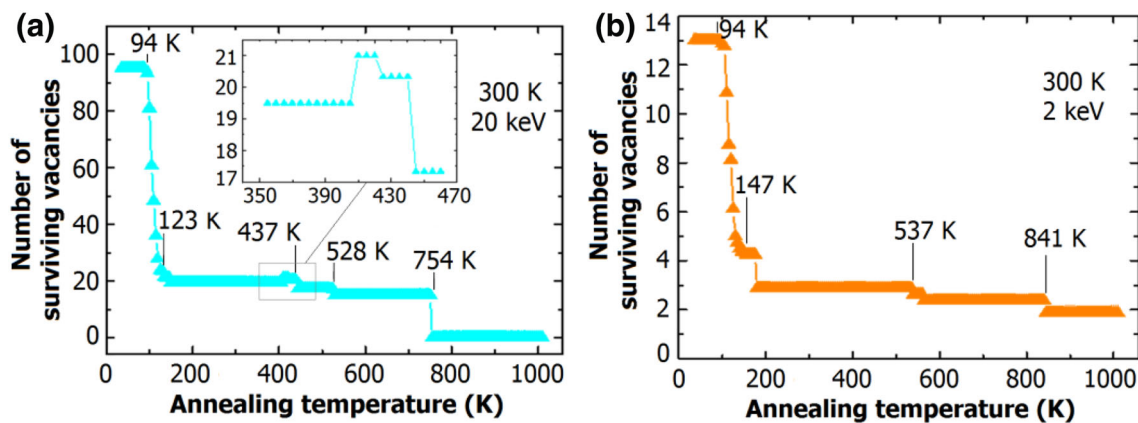


Fig. 5 Residual number of vacancies versus the annealing temperature, for primary defects at 300 K and $E_{PKA} = 2$ and 20 keV

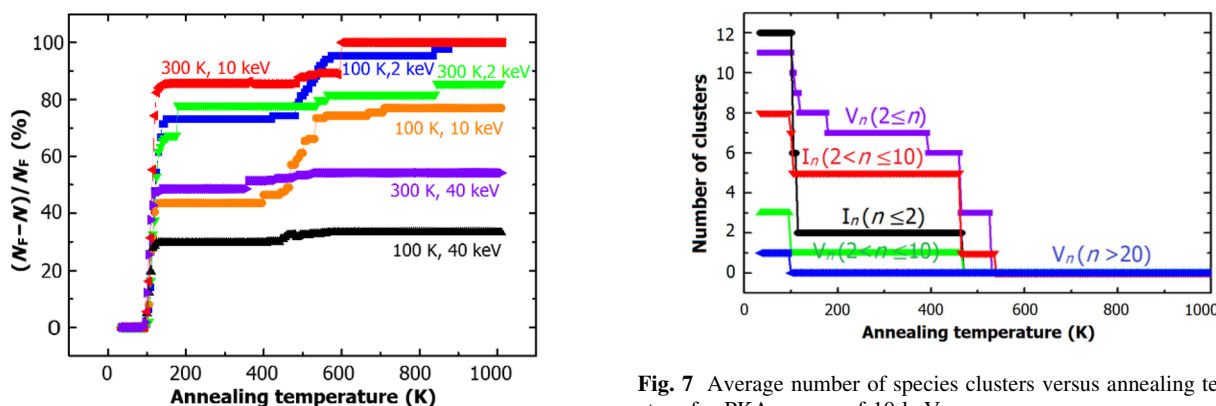


Fig. 6 Fraction of recovery defects as function of annealing temperature for $E_{PKA} = 2, 10$ and 40 keV

$E_{PKA} = 10$ keV are recombined before the annealing temperature goes to around 100 K, due to mainly the small size interstitial clusters migration along $\langle 111 \rangle$ direction. In particular, Stage I has several substages, because that as the annealing temperature increases, more small size vacancy clusters move and recombine with mobile interstitial clusters. Above 460 K, the recovery ratio fluctuates slightly because almost all small interstitial clusters are recombined and fewer mobile vacancy clusters breakaway from larger clusters. In Stage II, an additional 30% recombination ratio is added for cascade 2 and 10 keV at 100 K (cascade temperature). This is mainly due to the motion of residual small vacancy clusters and the emitting events during the annealing process. From Fig. 6, the fractions of surviving defects are 20–75% as Stage I ends, and 0–70% as the annealing ends. So, once again, the size and number distribution of clusters from the MD simulation can make a great difference in annealing simulation.

Figure 7 shows the average number of clusters for a 10 keV cascade, as the function of annealing temperature. It can be seen that a rapid drop of the number of small size interstitial clusters ($n \leq 2$) at the beginning of Stage I, and the number of

Fig. 7 Average number of species clusters versus annealing temperature for PKA energy of 10 keV

large size interstitial clusters ($2 < n \leq 10$) plunged. At this stage, large size vacancy clusters can be annihilated with the fast-moving interstitials clusters ($n \leq 2$), and the shrunken vacancy clusters further annihilate with large size interstitial clusters ($2 < n \leq 10$). Therefore, the results illustrate that the correlated recombination stage resulting from the motion of small interstitial clusters to a great extent. Also, the number of small vacancy clusters ($n \leq 2$) decreases, hence the occurrence of substages. At 460 K, at the uncorrelated recombination stage, the number of small size vacancy clusters ($n \leq 2$) and the large size interstitial clusters ($2 < n \leq 10$) begin to predominantly decline. This is due to the enhanced motion of small size vacancy clusters and increased possibility of emitting event. In addition, from the MD simulations, the interstitials prefer migrating along the $\langle 111 \rangle$ direction, but the high annealing temperature may change their preference and they may recombine with the vacancy clusters in the core.

4 Conclusion

MD and OKMC simulations were applied to investigate the displacement cascades and the evolution of irradiation-induced defects in Mo. The number of defect surviving

fraction was 0.02–0.05, indicating that most point defects recombined before annealing. Vacancy clusters were observed, and the $\langle 111 \rangle$ direction dumbbells were proved to be the most stable interstitials in Mo and could move along the $\langle 111 \rangle$ direction with low migration barriers (0.01–0.10 eV). Stage I at about 100 K was attributed to the correlated recombination, results from the motion SIAs ($n \leq 2$) to a great extent. The possibility of substage formation as due to the small vacancy clusters motion. In addition, a slight fluctuation was observed at 300–600 K. This was mainly due to the emitting events during the annealing. The size distribution of the clusters at the cascade quenching stage was positively correlated with the PKA energies, affecting notably the subsequent annealing process.

References

1. P. Yvon, F. Carré, Structural materials challenges for advanced reactor systems. *J. Nucl. Mater.* **385**, 217–222 (2009). doi:10.1016/j.jnucmat.2008.11.026
2. C. Jun, B.X. Xiao, C. Kun et al., Analysis on reactivity initiated transient from control rod failure events of a molten salt reactor. *Nucl. Sci. Tech.* **25**, 030602 (2014). doi:10.13538/j.1001-8042/nst.25.030602
3. A.A.F. Tavassoli, Present limits and improvements of structural materials for fusion reactors. *J. Nucl. Mater.* **302**, 73–88 (2002). doi:10.1016/S0022-3115(02)00794-8
4. P. Feng, S.Y. Liu, B. Wei et al., Simulation and experimental study of a random neutron analyzing system with ^{252}Cf neutron source. *Nucl. Sci. Tech.* **22**(1), 39–46 (2011). doi:10.13538/j.1001-8042/nst.22.39-46
5. T. Jun, J.X. Li, L.L. Tong et al., Core cooling in pressurized-water reactor during water injection. *Nucl. Sci. Tech.* **22**(1), 60–64 (2011). doi:10.13538/j.1001-8042/nst.22.60-64
6. Q. Han, Q.S. Wu, J.W. Chen et al., Analysis of fixation method of fuel assembly for lead-alloy cooled reactor. *Nucl. Sci. Technol.* **26**(5), 50601 (2015). doi:10.13538/j.1001-8042/nst.26.050601
7. G.D. Temmerman, M.J. Baldwin, R.P. Doerner et al., Beryllium deposition on international thermonuclear experimental reactor first mirrors: layer morphology and influence on mirror reflectivity. *J. Appl. Phys.* **102**, 083302 (2007). doi:10.1063/1.2798389
8. T. Sugie, S. Kasai, M. Taniguchi et al., Irradiation test of Mo- and W-mirrors for ITER by low energy deuterium ions. *J. Nucl. Mater.* **329–333**, 1481–1485 (2004). doi:10.1016/j.jnucmat.2004.04.248
9. B.V. Cockeram, J.L. Hollenbeck, L.L. Snead, The change in tensile properties of wrought LCAC molybdenum irradiated with neutrons. *J. Nucl. Mater.* **324**, 77–89 (2004). doi:10.1016/j.jnucmat.2003.05.001
10. M.M. Li, M. Eldrup, T.S. Byun et al., Low temperature neutron irradiation effects on microstructure and tensile properties of molybdenum. *J. Nucl. Mater.* **376**, 11–28 (2008). doi:10.1016/j.jnucmat.2007.12.001
11. D. Yun, M.A. Kirk, P.M. Baldo et al., In situ TEM investigation of Xe ion irradiation induced defects and bubbles in pure molybdenum single crystal. *J. Nucl. Mater.* **437**, 240–249 (2013). doi:10.1016/j.jnucmat.2013.01.305
12. D.H. Xu, B.D. Wirth, M.M. Li et al., Defect micro-structural evolution in ion irradiated metallic nano-foils: Kinetic Monte Carlo simulation versus cluster dynamics modeling and in situ transmission electron microscopy experiments. *Appl. Phys. Lett.* **101**, 101905 (2012). doi:10.1063/1.4748980
13. M. Eldrup, M.M. Li, L.L. Snead et al., Characterization of defect accumulation in neutron-irradiated Mo by positron annihilation spectroscopy. *Nucl. Instrum. Methods B* **266**, 3602–3606 (2008). doi:10.1016/j.nimb.2008.06.018
14. A.Y. Kuksin, G.E. Norman, V.V. Stegailov et al., Radiation-induced damage and evolution of defects in Mo. *Phys. Rev. B* **84**, 104109 (2011). doi:10.1103/PhysRevB.84.104109
15. S. Han, L.A. Zepeda-Ruiz, G.J. Ackland et al., Self-interstitials in V and Mo. *Phys. Rev. B* **66**, 220101 (2002). doi:10.1103/PhysRevB.66.220101
16. Young, F.W. and Jr., What do we really know about the atomic-scale structures of nanophase materials. *J. Nucl. Mater.* **310**, 69–70 (1978). doi:10.1016/0022-3697(94)90127-9
17. D.N. Manh, A.P. Horsfield, S.L. Dudarev, Self-interstitial atom defects in bcc transition metals: Group-specific trends. *Phys. Rev. B* **73**, 020101 (2006). doi:10.1103/PhysRevB.73.020101
18. A.F. Calder, D.J. Bacon, A.V. Barashev et al., On the origin of large interstitial clusters in displacement cascades. *Philos. Mag* **863**, 90 (2010). doi:10.1080/14786430903117141
19. A.P. Selby, D.H. Xu, N. Juslin et al., Primary defect production by high energy displacement cascades in molybdenum. *J. Nucl. Mater.* **437**, 19–23 (2013). doi:10.1016/j.jnucmat.2013.01.332
20. F. Gao, D.J. Bacon, A.V. Barashev et al., Modeling the long-term evolution of the primary damage in ferritic alloys using coarse-grained methods. *Mat. Res. Soc. Symp. Proc* **540**, 703–708 (1999). doi:10.1016/j.jnucmat.2010.05.019
21. T. Suzudo, S.I. Golubov, R.E. Stoller et al., Annealing simulation of cascade damage in $\alpha\text{-Fe}$ —Damage energy and temperature dependence analyses. *Proc. Nucl. Sci. Tech.* **2**, 56–63 (2011). doi:10.1016/j.jnucmat.2012.01.014
22. H.L. Heinisch, B.N. Singh, Stochastic annealing simulation of intracascade defect interactions. *J. Nucl. Mater.* **251**, 77–85 (1997). doi:10.1016/S0022-3115(97)00219-5
23. A. Almazouzi, M.J. Caturla, T.D. Rubia et al., Annealing kinetics of single displacement cascades in Ni: an atomic scale computer simulation. *Mat. Res. Soc. Symp. Proc* **540**, 685–690 (1999). doi:10.1557/PROC-540-685
24. Z.W. Rong, F. Gao, W.J. Weber, Monte Carlo simulations of defect recovery within a 10 keV collision cascade in 3C–SiC. *J. Appl. Phys* **102**, 103508 (2007). doi:10.1063/1.2812701
25. H.L. Heinisch, B.N. Singh, Stochastic annealing simulation of differential defect production in high energy cascades. *J. Nucl. Mater.* **232**, 206–213 (1996). doi:10.1016/S0022-3115(96)00434-5
26. K. Wang, H.Q. Deng, W.Y. Hu et al., An atomic study on the shock-induced plasticity and phase transition for iron-based single crystals. *Int. J. Plast* **59**, 180–198 (2014). doi:10.1016/j.ijplas.2014.03.007
27. N.W. Hu, S.F. Xiao, H.Q. Deng et al., Molecular dynamics simulation of displacement cascades in Ni–Mo alloy. *Nucl. Sci. Tech.* **26**, 060603 (2015). doi:10.13538/j.1001-8042/nst.26.060603
28. P. Maragakis, S.S.A. Andreev, Y. Brumer et al., Adaptive nudged elastic band approach for transition state calculation. *J. Chem. Phys* **117**, 4651 (2002). doi:10.1063/1.1495401
29. J.W. Chu, B.L. Trout, B.R. Brooks, A super-linear minimization scheme for the nudged elastic band method. *J. Chem. Phys* **119**, 12708 (2003). doi:10.1063/1.1627754
30. G. Henkelman, B.P. Uberuaga, H. Jónsson, A climbing image nudged elastic band method for finding saddle points and minimum energy paths. *J. Chem. Phys* **113**, 9901 (2000). doi:10.1063/1.1329672
31. C.S. Becquart, C. Domain, An object kinetic Monte Carlo Simulation of the dynamics of helium and point defects in tungsten.

- J. Nucl. Mater. **385**, 223–227 (2009). doi:[10.1016/j.jnucmat.2008.11.027](https://doi.org/10.1016/j.jnucmat.2008.11.027)
32. G.J. Galloway, G.J. Ackland, Molecular dynamics and object kinetic Monte Carlo study of radiation-induced motion of voids and He bubbles in bcc iron. *Phys. Rev. B* **87**, 104106 (2013). doi:[10.1103/PhysRevB.87.104106](https://doi.org/10.1103/PhysRevB.87.104106)
33. R.E. Stoller, S.I. Golubov, C. Domain et al., Mean field rate theory and object kinetic Monte Carlo: a comparison of kinetic models. *J. Nucl. Mater.* **382**, 77–90 (2008). doi:[10.1016/j.jnucmat.2008.08.047](https://doi.org/10.1016/j.jnucmat.2008.08.047)
34. J. Yang, Y. Yang, Y. Li et al., Monte-Carlo simulation of cement neutron field distribution characteristics in PGNAA. *Nucl. Sci. Tech.* **6**, 006 (2012). doi:[10.13538/j.1001-8042/nst.23.337-343](https://doi.org/10.13538/j.1001-8042/nst.23.337-343)
35. L. Gámez, B. Gámez, M.J. Caturla et al., Object Kinetic Monte Carlo calculations of irradiated Fe–Cr dilute alloys: the effect of the interaction radius between substitutional Cr and self-interstitial Fe. *Nucl. Instrum. Methods B* **269**, 1684–1688 (2011). doi:[10.1016/j.nimb.2010.12.044](https://doi.org/10.1016/j.nimb.2010.12.044)
36. C. Domain, C.S. Becquart, L. Malerba, Simulation of radiation damage in Fe alloys: an object kinetic Monte Carlo approach. *J. Nucl. Mater.* **335**, 121–145 (2004). doi:[10.1016/j.jnucmat.2004.07.037](https://doi.org/10.1016/j.jnucmat.2004.07.037)
37. T. Suzudo, S.I. Golubov, R.E. Stoller et al., Kinetic Monte Carlo annealing simulation of cascade damage in α -Fe. *Pro. Nuc. Sci. Tec* **2**, 56–63 (2011). doi:[10.15669/pnst.2.56](https://doi.org/10.15669/pnst.2.56)
38. H.X. Xu, Y.N. Osetsky, R.E. Stoller, Cascade annealing simulations of bcc iron using object kinetic Monte Carlo. *J. Nucl. Mater.* **423**, 102–109 (2012). doi:[10.1016/j.jnucmat.2012.01.020](https://doi.org/10.1016/j.jnucmat.2012.01.020)
39. C.C. Fu, J.D. Torre, F. Willaime et al., Multiscale modelling of defect kinetics in irradiated iron. *Nat. Mat.* **4**, 68–74 (2005). doi:[10.1038/nmat1286](https://doi.org/10.1038/nmat1286)
40. D.J. Bacon, F. Gao, Y.N. Osetsky, Computer simulation of displacement cascades and the defects they generate in metals. *Nucl. Instrum. Methods B* **153**, 87–98 (1999). doi:[10.1016/S0168-583X\(99\)00041-5](https://doi.org/10.1016/S0168-583X(99)00041-5)
41. R.A. Johnson, Interstitials and vacancies in α iron. *Phys. Rev.* **134**, 5 (1964). doi:[10.1103/PhysRev.134.A1329](https://doi.org/10.1103/PhysRev.134.A1329)
42. G.J. Galloway, G.J. Ackland, Molecular dynamics and object kinetic Monte Carlo study of radiation-induced motion of voids and He bubbles in bcc iron. *Phys. Rev. B* **87**, 104106 (2013). doi:[10.1103/PhysRevB.87.104106](https://doi.org/10.1103/PhysRevB.87.104106)